Crystal growth of $Sr_2Ir_xRu_{1-x}O_4$ for $x \leq 0.4$

Zach Porter[a], Eli Zoghlin[a], Julian L. Schmehr[a], Stephen D. Wilson[a,b,*]

[a] *Materials Department, University of California, Santa Barbara, California 93106, USA*
[b] *California NanoSystems Institute, University of California, Santa Barbara, California 93106, USA*

Abstract

We describe the synthesis of crystalline $Sr_2Ir_xRu_{1-x}O_4$ via a floating zone growth technique. We find that the use of a high pressure gas environment (70 bar mixed O_2 and Ar) greatly decreases the volatility and loss of the IrO_2 and RuO_2 reactants. The resultant gram-sized samples are more uniform in composition than comparable flux-grown crystals.

Keywords: A1. Crystal structure, A2. Floating zone technique, A2. Growth from melt, B1. Alloys, B1. Perovskites, B2. Magnetic materials

1. Introduction

$Sr_2Ir_xRu_{1-x}O_4$ is an alloy of the single layer member of the Ruddlesden-Popper series; its chemical formula is $Sr_{n+1}(Ir,Ru)_nO_{3n+1}$ with n=1. It consists of alternating layers of SrO rock salt and perovskite, such that there are separated planes of corner-sharing $(Ir,Ru)^{4+}O_6^{2-}$ octahedra. This correlated $5d/4d$ transition metal oxide material system lies within a rich, yet largely unexplored, magnetic phase diagram with predictions of strange-metal behavior and magnetic quantum criticality. The parent ruthenate, Sr_2RuO_4, is a widely studied unconventional superconductor [1, 2]. Its $\mathbf{S}$=1 ground state is paramagnetic, although the system possesses weak spin fluctuations with wave vector $(\pm\pi/3a, \pm\pi/3a, 0)$ in its normal correlated metal state [3, 4]. In contrast, the fully Ir-substituted system Sr_2IrO_4 is a $\mathbf{J}_{\text{eff}}$=1/2 Mott insulator with long-range G-type antiferromagnetic (AF) order [5].

An open question regarding the phase diagram is how moderate levels of Ir substitution affect the magnetic ground state and lattice symmetry of Sr_2RuO_4. Sr_2RuO_4 is known to possess a metallic state near a critical phase boundary where dilute substitution of elements on the Ru site can drive it into a magnetically ordered phase. This transition occurs for dopants both with [6, 7, 8] and without [9] evident charge doping or magnetic impurities. Recently, an ARPES study has demonstrated two Lifshitz transitions in the doping series $Sr_2Ir_xRu_{1-x}O_4$ for x=0.15(5) and 0.45(5), which are expected to yield novel electronic or magnetic phase behavior and possibly quantum criticality [10]. Motivated by this result and related previous work, we endeavored to improve experimental efforts on unconventional correlated metal phases in $Sr_2Ir_xRu_{1-x}O_4$ by improving the sample quality and volume of crystals in the alloy series. Crucially, floating zone synthesis fully opens this class of materials to study via neutron scattering, which enables more thorough investigation of O positions, magnetic structure, and excitations than previous work on smaller crucible-based flux-

*Please address correspondence to
Email address: stephendwilson@ucsb.edu (Stephen D. Wilson)

grown crystals. Floating zone synthesis also has the potential to improve the alloy homogeneity due its ability to actively mix the melt during the crystal growth process.

In this paper, we describe the results of growth of $Sr_2Ir_xRu_{1-x}O_4$ crystals with $0 \leq x \leq 0.4$ on the Ru-rich side of the solid solution between Sr_2IrO_4 and Sr_2RuO_4. We discuss the evolution of the average structure of crystals in the alloy series, and additionally, we report on composite two-phase structures that form under certain conditions. They include lamellae of (Ir,Ru) metal alloy, and also dendrites of a seemingly metastable phase $Sr_9(Ir,Ru)_3O_{17}$, both embedded in the bulk phase.

2. Materials and Methods

Crystals of $Sr_2Ir_xRu_{1-x}O_4$ were grown with a floating zone (FZ) technique with an $(Ir,Ru)O_2$ self-flux. In our apparatus, we first melt the tip of the seed rod (affixed from below) and then lower the feed rod (suspended from above) into the melt, establishing a connected molten zone. We pull a crystal from the $(Ir,Ru)O_2$-rich molten solution by lowering both rods through the fixed optical heating source. For this work we used a custom furnace with a laser-based heating source designed to accommodate high gas pressures, which is described elsewhere [11]. The relevant details of the furnace are that the molten zone is approximately 4 mm tall and 6-7 radially distributed laser beams are used to heat the zone with an optical wavelength in the range 800-820 nm.

Polycrystalline seed and feed rods were prepared via solid-state reaction. $SrCO_3$ (99.99% excluding Ca or Ba) and IrO_2 (99.99% metals basis) and RuO_2 (99.95% metals basis) were used as starting materials, all sourced from Alfa Aesar. We found some as-purchased IrO_2 and RuO_2 powders to be O-deficient, so these precursors were initially heated in a tube furnace to 700 °C for 18 h with O_2 flow at 30 SCCM to ensure full O occupation. The IrO_2 and RuO_2 were dried at 700 °C, and the $SrCO_3$ was dried at 400 °C for at least 18 h in air prior to weighing. The input stoichiometries are reported in Table 1.

To prepare the initial powder, reagents were mixed in an agate mortar, packed into a clean latex balloon, and pressed into a pellet at 300 MPa within an isostatic press. The pelletized powder was then removed from the balloon, placed in an alumina crucible on a thick layer of reactant powder, and sintered at 1100 °C for 18 h in air. Polycrystalline feed rods were prepared from the resulting powder, by regrinding the sintered pellet into powder and tightly and uniformly packing the powder into a water-cleaned cylindrical latex balloon with diameter 5 mm and length up to 120 mm. The packed balloon was then evacuated, straightened, wrapped tightly with paper, and pressed at 300 MPa for 3 minutes. The rod was removed from the balloon and sintered at 1380 °C for up to 12 h in air on a conforming bed of reactant powder. Polycrystalline rod density was typically near 72(5)%; density of pure ruthenate rods was reported as "low" in Ref. [12], and similar sintering conditions were used in other more recent synthetic efforts [13].

For the FZ growth procedure, the seed and feed rods were initially aligned to minimize rod precession. Next the chamber was sealed and pressurized. Optical power was increased over approximately 40 minutes to gradually heat the seed's tip. When the seed became molten (nearly 2150 °C) the feed rod was lowered slowly to establish a connected molten zone. The seed and feed rods were counter-rotated at ≈10 rpm. The low surface tension and/or melt viscosity required a lower translation speed for the feed rod relative to the seed rod in order to keep the zone stable; i.e. the volumetric flow rate into the zone was less than the rate of the crystal pulled out, as others reported for Sr_2RuO_4 e.g. Refs. [13, 14]. This caused the crystal boule's diameter to be less than the polycrystalline rod's diameter. As such, the zone narrowed after the initial join, so

the power and translation speeds were adjusted after the beginning of the growth. We report the final values of these parameters for the crystal growth in Table 1. When the growth was complete, the molten zone was disconnected and the optical power was ramped down slowly. The 'as-grown' crystals were removed from the furnace and a subset were subsequently annealed in air on powder beds for 4 to 6 days at 1380 °C. Such samples are indicated as 'annealed' within this report.

Regarding damage to the furnace, our syntheses did not affect the thick and chemically resistant Inconel 718 growth chamber walls or the CuBe inner shielding pieces. The evaporation did slightly discolor the quartz inner shroud which is closest to the growth zone, but each shroud was usable for about 10 such syntheses before the absorption effects were noticeable.

Preliminary powder x-ray diffraction (PXRD) was performed with a Panalytical Empyrean diffractometer using lab-source Cu K-α radiation, and follow-up high-resolution synchrotron measurements were taken at Beamline 11-BM of the Advanced Photon Source at Argonne National Laboratory with a fixed wavelength of 0.458 Å. The PXRD patterns were refined using the TOPAS software package. We oriented crystals and assessed the crystal quality with a Photonic Science back reflection Laue Crystal Orientation System. Additionally, a ThermoFisher Apreo C scanning electron microscope was utilized for energy-dispersive x-ray spectroscopy (EDX) and backscattered electron imaging (BSE) with a typical configuration of 20 kV accelerating voltage and 1.6 nA beam current.

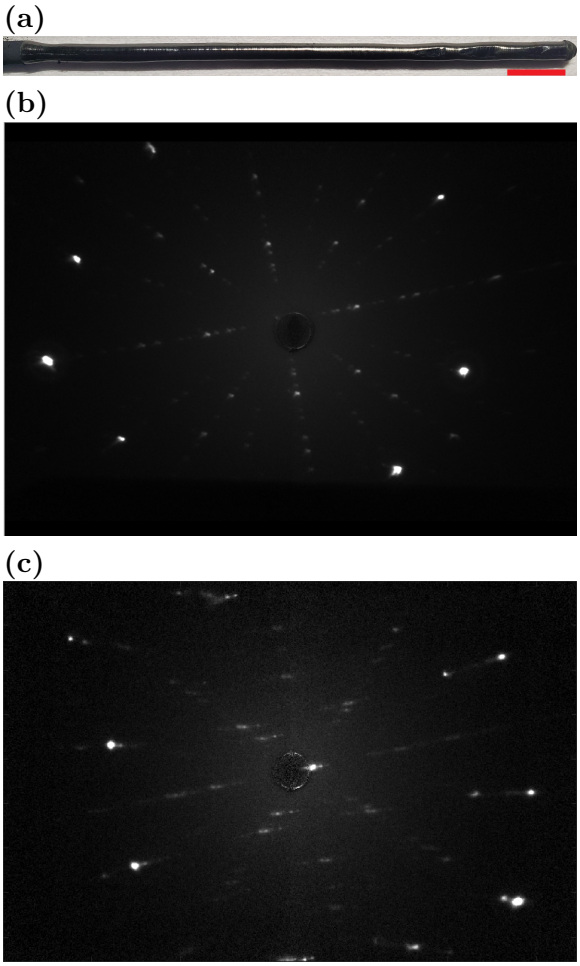

Figure 1: (a) Photograph of a representative sample: batch 'x0.25c'. Exterior facets are visible toward the end of the growth (right). The red scale bar is 1 cm. (b,c) Backscattered Laue detector images of cleaved surfaces of annealed $Sr_2Ir_xRu_{1-x}O_4$ for (b) batch 'x0.10c' and (c) batch 'x0.40c' confirm that they are crystalline. The samples are mounted with the growth direction vertical and c approximately along the beam, so the rotation of the patterns indicates that the a axis is 10-15 degrees away from the growth direction. The sample in (c) is more mosaic due to the oxidizing synthesis environment.

3. Results

3.1. Crystal growth and characterization

Nearly phase-pure samples were produced by optimizing the sample stoichiometry and the gas environment used during crystal growth.

batch	x_{nom}	x	input stoichiometry	RuO_2 excess [mol%]	IrO_2 excess [mol%]	P_{melt} [W]	P_{end} [W]	p_{O_2} [bar]	p_{Ar} [bar]	v_{feed} [mm/h]	v_{seed} [mm/h]	as-grown (Ir,Ru) [wt%]	as-grown '9-3-17' [wt%]	annealed (Ir,Ru) [wt%]
x0a	0	-	$Sr_2Ir_{0.00}Ru_{1.03}O_{4.1}$	3	-	210	198	3	66	33	40	0.6	-	
x0.10a	0.10	0.09	$Sr_2Ir_{0.12}Ru_{0.93}O_{4.1}$	3	2	210	216	3	66	35	40	1.1	-	
x0.10b	0.10	0.08	$Sr_2Ir_{0.11}Ru_{0.93}O_{4.1}$	3	1	234	228	3	66	35	40	0.1	-	
x0.10c	0.10	0.09	$Sr_2Ir_{0.10}Ru_{0.91}O_{4.1}$	1	0	240	228	3	66	33	40	0.1	-	0.1
x0.15a	0.15	0.15	$Sr_2Ir_{0.17}Ru_{0.86}O_{4.1}$	1	2	234	228	3	66	32	40	1.2	-	0.7
x0.18a	0.18	0.18	$Sr_2Ir_{0.20}Ru_{0.83}O_{4.1}$	1	2	234	228	3	66	55	40	0.1	-	0.1
x0.20a	0.20	0.20	$Sr_2Ir_{0.23}Ru_{0.81}O_{4.1}$	1	3	276	252	14	55	25	40	0.1	3.5	0.1
x0.20b	0.20	0.20	$Sr_2Ir_{0.23}Ru_{0.81}O_{4.1}$	1	3	300	276	3	66	25	40	0.2	-	0.2
x0.25a	0.25	0.23	$Sr_2Ir_{0.26}Ru_{0.76}O_{4.1}$	1	1	240	240	3	66	34	40	0.5	-	
x0.25b	0.25	0.23	$Sr_2Ir_{0.28}Ru_{0.76}O_{4.1}$	1	3	240	222	3	66	36	40	0.7	-	
x0.25c	0.25	0.24	$Sr_2Ir_{0.28}Ru_{0.76}O_{4.1}$	1	3	240	240	3	66	31	40	0.9	-	0.9
x0.32a	0.32	0.32	$Sr_2Ir_{0.37}Ru_{0.69}O_{4.1}$	1	5	282	264	14	55	29	40	0.2	-	0.2
x0.40a	0.40	0.31	$Sr_2Ir_{0.41}Ru_{0.61}O_{4.1}$	1	1	264	276	3	66	32	40	2.1	8.1	
x0.40b	0.40	0.38	$Sr_2Ir_{0.46}Ru_{0.61}O_{4.1}$	1	6	258	252	3	66	33	40	3.0	6.9	
x0.40c	0.40	0.39	$Sr_2Ir_{0.46}Ru_{0.61}O_{4.1}$	1	6	276	258	14	55	34	40	0.1	4.0	0.1

Table 1: Crystal growth parameters: batch name, nominal and EDS-measured Ir substitution x, input stoichiometry, excess reactant, total beam power during melting and at the end of the growth P, partial pressure p, feed and seed translation speed v. The last columns contain the impurity phase fractions of the (Ir,Ru) alloy and the '9-3-17' phase $Sr_9(Ir,Ru)_3O_{17}$ as attained from laboratory PXRD refinements before and after annealing crystals at 1380 °C for 4 to 6 days in air. Note that as-grown and annealed samples are ground from similar regions of the boule but are not the same samples, which accounts for some of the variation in alloy phase fraction.

Other growth parameters throughout the series of samples were held fixed, to the best of our ability. A typical image of an as-grown $Sr_2Ir_xRu_{1-x}O_4$ boule is shown in Figure 1a. A crystal grain is typically selected within 2 cm of growth when seeded from a polycrystalline rod, as evidenced by facets on the exterior and interior of the boule and confirmed by Laue measurements (Figure 1b,c). As observed for the parent compound Sr_2RuO_4, the $(Ir,Ru)O_2$ layer direction (*ab* basal plane) is typically along the growth direction (cylinder axis)[12, 13]. Samples readily cleave along the basal plane.

For consistency, a fixed chamber pressure of 69(4) bar at room temperature was used. The optimal gas environment in our syntheses was found to be a ratio of 96:4 $Ar:O_2$. For several syntheses of samples with higher Ir content, a more oxidizing environment with a ratio of 80:20 $Ar:O_2$ was utilized to decrease the Ir metal content. This led to high-phase-purity samples but also resulted in crystals that are highly friable and exfoliate easily. The gas environment for each growth attempt for an array of Ir concentrations is shown in Table 1.

To prepare the nominal chemical formula $Sr_2Ir_xRu_{1-x}O_4$, the optimal input stoichiometry contains 15 mol% excess IrO_2 and 1 mol% excess RuO_2; that is, $Sr_2Ir_{1.15x}Ru_{1.01(1-x)}O_{4.02+0.28x}$. The input stoichiometries and reactant excess values are summarized in Table 1; some batch stoichiometries are not optimal. Note that, at lower pressures, earlier reports required far greater excesses of IrO_2 and RuO_2 within starting stoichiometries. For example, in a FZ study by N. Kikugawa and co-workers with Ir $x \leq 3\%$ grown in 2.2 bar of 90:10 $Ar:O_2$, the reported starting stoichiometry contains an excess of about 300 mol% IrO_2 and 15 mol% RuO_2 [15].

For the samples reported here, there are two impurities detected via powder x-ray diffraction collected on crushed crystals. The first is an alloy of Ir and Ru that, for samples with $x>0$, adopts the Ir $Fm\bar{3}m$ space group. The second phase appears as an Ru-substituted

form of the recently reported phase $Sr_9Ir_3O_{17}$ [16]. Electron microscopy for these impurities is shown in Figure 4 and discussed later.

In Table 1 we summarize growth parameters for a variety of trial growths and the composition of the resulting boules. We note that the variance in the feed translation speed compensates for differences in the feed density and diameter. The required power for melting is a relative metric only and depends on a number of parameters; however the overall trend is to increase with Ir content. We do not report the pyrometer-measured temperature because it primarily varies with the pyrometer reticle position and with the amount of volatilized powder that coats the sapphire inner shroud in front of the pyrometer.

The evolution of the bulk crystallographic parameters across the substitution series is shown in Table 2 and lattice parameters are plotted in Figure 2. The samples are indexed to the $I4/mmm$ tetragonal space group commonly used for Sr_2RuO_4, and the atomic displacement parameters increase with x as expected for substitutional disorder. While the out-of-plane lattice constant c trends up with x, the in-plane lattice constant a only weakly depends on x.

There are two free coordinates for this compound in the $I4/mmm$ space group, O(2) z and Sr(1) z; both are 4e Wyckoff positions with $x = y = 0$. These free coordinates parameterize the positions of the apical O ions and Sr ions along c. In the refinements, the O(2) z positions are unreliable, but there is a weak trend down in Sr(1) z with increasing x, which indicates that Sr ions are positioned farther away from the (Ir,Ru)O_2 planes with Ir content. In other words there is a small Jahn-Teller elongation with increasing x.

The volumetric thermal expansion is positive for all samples. Interestingly, there is a changeover in the coefficient of thermal expansion along c, from thermal expansion for x=0 and 0.09 to thermal contraction for x=0.24 and 0.39 − see Figure 2. This change is likely related to oxygen octahedral rotations and may indicate a subtle symmetry change that we do not observe in laboratory PXRD at room temperature. There is an unindexed peak in the synchrotron PXRD for the x=0.24 and 0.39 samples near Q=2.55 Å^{-1} that is stronger at 100 K than at 295 K. This may be the disallowed (1 1 2) peak which is allowed for the Sr_2IrO_4 $I4_1/acd$ space group. Future neutron diffraction studies will help to clarify the nature of this peak and the thermal contraction of the c-axis .

batch		x0a	x0.10c	x0.25c	x0.40c
$x_{\rm nom}$		0	0.10	0.25	0.40
x		0	0.09	0.24	0.39
100 K					
a	[Å]	3.8641	3.8673	3.8641	3.8638
c	[Å]	12.730	12.733	12.806	12.848
Sr(1) z		0.3536	0.3536	0.3519	0.3513
O(2) z		0.161	0.162	0.169	0.167
Sr U_{iso}	[Å^2]	0.004	0.004	0.003	0.005
B U_{iso}	[Å^2]	0.003	0.003	0.004	0.006
$R_{\rm wp}$	[%]	9.79	8.06	8.61	10.22
χ^2		1.15	1.50	1.25	1.61
295 K					
a	[Å]	3.8716	3.8757	3.8749	3.8749
c	[Å]	12.746	12.741	12.791	12.830
Sr(1) z		0.3535	0.3535	0.3522	0.3512
O(2) z		0.160	0.164	0.168	0.169
Sr U_{iso}	[Å^2]	0.007	0.008	0.007	0.006
B U_{iso}	[Å^2]	0.004	0.005	0.007	0.009
$R_{\rm wp}$	[%]	9.76	8.88	9.14	10.51
χ^2		1.19	1.35	1.19	1.09

Table 2: Select bulk crystallographic data from Rietveld refinement of synchrotron PXRD data on as-grown samples. First, batch name, nominal and measured x from EDS measurements. Next, refined values at 100 K and at 295 K: a and c tetragonal lattice parameters; Sr(1) z and the O(2) z free parameters; isotropic atomic displacement parameters U_{iso} for the Sr and B sites (B=Ir/Ru); and Rietveld goodness-of-fit parameters $R_{\rm wp}$ and χ^2. Note all occupancies were set to the stoichiometric values. U_{iso} for oxygen sites was fixed at 0.008 Å. The O(2) z positions are not reliable in that their refined positions have minimal effects on the goodness-of-fit, because the x-ray diffraction signal is dominated by the heavier elements. If not indicated, uncertainties are smaller than half of the last significant digit.

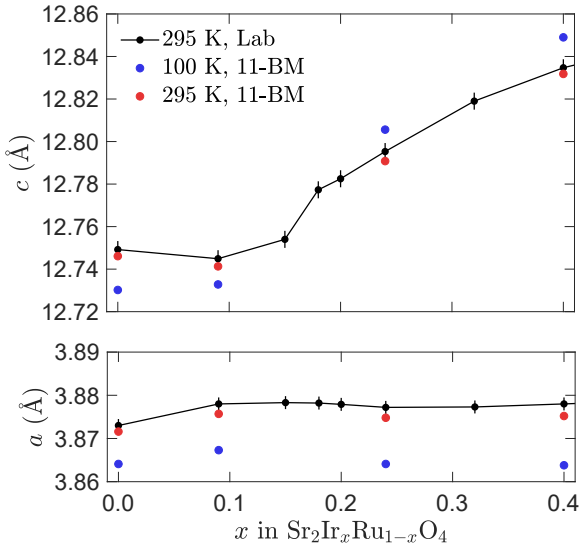

Figure 2: Tetragonal lattice parameters from PXRD refinements. Lab-source data (black) is indicated as 'Lab' and synchrotron data is indicated as '11-BM' in the figure. Approximate uncertainties are either indicated with error bars or are smaller than the data markers. Lines are a guide to the eye.

The homogeneity of the Ir substitution x was measured with EDX mapping. The Ir/Ru atomic ratios are homogeneous on the ∼10 μm scale; i.e. the variation in x is within measurement uncertainty $\sigma_x \approx 0.2\%$. The variation in x on the ∼5 mm scale (i.e. radially across the crystal boule) is within $\sigma_x \leq 0.5\%$.

This alloy homogeneity for FZ-synthesized samples is an improvement compared to previously reported flux-synthesized samples. In the ARPES study on the same compound grown via a flux method by J. Kwon and co-workers, the reported EDX-measured variance in x is about 3% on the 100 μm scale [10]. This value is consistent with measurements reported on the related compound $Sr_3(Ir,Ru)_2O_7$, for which the variation in x for the highest-quality flux samples is typically near 2% on both the μm and mm length scales - see e.g. Ref. [17].

3.2. Impurity phases

We now comment on impurity phases that result and are amplified away from optimal

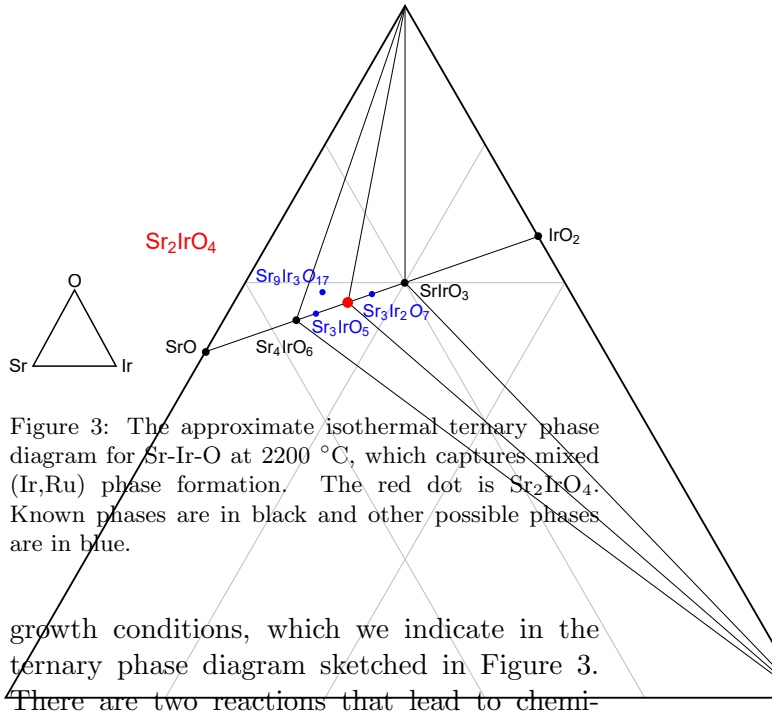

Figure 3: The approximate isothermal ternary phase diagram for Sr-Ir-O at 2200 °C, which captures mixed (Ir,Ru) phase formation. The red dot is Sr_2IrO_4. Known phases are in black and other possible phases are in blue.

growth conditions, which we indicate in the ternary phase diagram sketched in Figure 3. There are two reactions that lead to chemical inhomogeneity and likely drive unwanted phase formation: (a) $(Ir,Ru)O_2$ reduces to form (Ir,Ru) metal just below the liquidus temperature[18] and also (b) $(Ir,Ru)O_2$ reacts with oxygen gas to briefly form $(Ir,Ru)O_{3,4}(g)$, which effectively evaporates the oxide from the molten zone.

The small (typically <1 wt%) (Ir,Ru) metal impurity detected in diffraction measurements is primarily caused by the reduction of the oxides, during both the solid state reaction as well as during FZ growth. The observed ∼1 μm size lamellar alloy formation in unannealed samples is shown in Figure 4. The alloy is predominantly Ir even for low Ir content, and EDS measurements indicate compositions of $Ir_{0.85}Ru_{0.15}$ for the $x \approx 0.1$ batches and closer to $Ir_{0.95}Ru_{0.05}$ for samples with $x \approx 0.2$.

In unannealed samples, a perovskite-like impurity phase is identified most closely matching the structure of $Sr_9(Ir,Ru)_3O_{17}$ as seen in Figure 4b. Our diffraction data are most consistent with this phase and unannealed samples show a weak 11 K feature in susceptibility (not shown) resembling the reported antiferromagnetism of $Sr_9Ir_3O_{17}$. An alternative model for this impurity phase could be $Sr_3(Ir,Ru)O_{5+\delta}$ (related to double perovskites like Sr_3WO_6 but with O vacancies [14]). For visualization these phases are included in the ternary phase diagram Figure 3. This phase disappears upon annealing, suggesting it is metastable. The phase

fraction of this impurity scales with excess Ir content in unannealed crystals, and it seems to form upon rapid cooling in locally Ir/Ru poor regions in an oxidizing environment - see Ref. [14].

Other Ruddlesden-Popper phases such as the bilayer $Sr_3(Ir,Ru)_2O_7$ and the trilayer $Sr_4(Ir,Ru)_3O_{10}$ compounds were not observed in PXRD or SEM measurements. However, a dilute quantity <0.1 mol% of the ferromagnetic $Sr(Ir,Ru)O_3$ phase is detectable solely via magnetization data. This perovskite phase is also not directly visible in PXRD or SEM data, similar to reports on the parent system Sr_2RuO_4 [14]. It has a ferromagnetic ground state with a saturated moment as high as 1.5 μ_B per Ru ion, so even ppm impurities of $Sr(Ir,Ru)O_3$ can be resolved via low-field magnetization measurements [19, 20].

4. Conclusions

The FZ growth of large, homogeneous $Sr_2Ir_xRu_{1-x}O_4$ crystals is reported. By leveraging a high pressure gas environment, the IrO_2 and RuO_2 losses are suppressed by more than a factor of 10 compared to previous reports. This enables the stable growth of alloy compositions with high Ir content. Crystals were created for $x \leq 0.4$ and the impurity phases that intermix away from optimal growth/annealing conditions were analyzed. Our findings motivate the pursuit of compositions of $Sr_2Ir_xRu_{1-x}O_4$ with higher Ir content as well as the exploratory crystal growth of other compounds with volatile constituents via high pressure floating zone techniques.

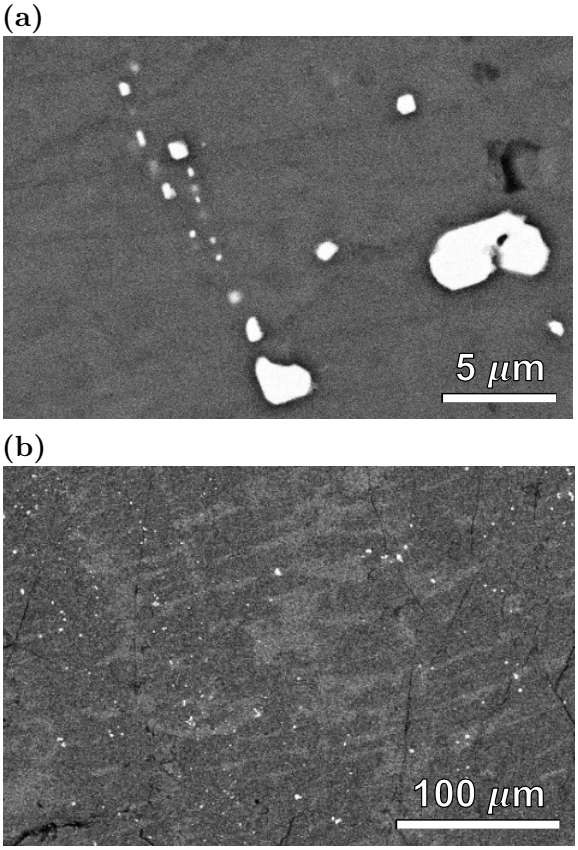

Figure 4: Scanning electron microscope backscattered electron images for polished as-grown samples: (a) batch 'x0.10b' with inclusions and lamellae of the (Ir,Ru) alloy phase that appears brighter than the bulk; and (b) batch 'x0.40a' which additionally contains a dendritic phase that appears slightly brighter than the bulk. The Sr:(Ir,Ru) ratio of this phase is near 3:1 from EDX analysis.

Acknowledgements

We thank Brenden R. Ortiz and Qingbiao Zhao for helpful discussions, and Ludwig Holleis and Andrea F. Young for assistance with resistivity measurements. S.D.W., Z.P., and E.Z. acknowledge support from NSF Grant

No. DMR-1905801. This work used facilities supported via the UC Santa Barbara NSF Quantum Foundry funded via the Q-AMASE-i program under award DMR-1906325. This research made use of the shared facilities of the NSF Materials Research Science and Engineering Center at UC Santa Barbara, Grant No. DMR-1720256. We acknowledge the use of the Nanostructures Cleanroom Facility within the California NanoSystems Institute, supported by the University of California, Santa Barbara and the University of California, Office of the President. Use of the Advanced Photon Source at Argonne National Laboratory was supported by the U. S. Department of Energy, Office of Science, Office of Basic Energy Sciences, under Contract No. DE-AC02-06CH11357.

References

[1] A. P. Mackenzie, T. Scaffidi, C. W. Hicks, Y. Maeno, Even odder after twenty-three years: The superconducting order parameter puzzle of Sr_2RuO_4, npj Quantum Materials 2 (1) (2017) 1–9. doi:10.1038/s41535-017-0045-4.

[2] A. J. Leggett, Y. Liu, Symmetry properties of superconducting order parameter in Sr_2RuO_4, Journal of Superconductivity and Novel Magnetism 34 (6) (2021) 1647–1673. doi:10.1007/s10948-020-05717-6.

[3] Y. Sidis, M. Braden, P. Bourges, B. Hennion, S. Nishi Zaki, Y. Maeno, Y. Mori, Evidence for incommensurate spin fluctuations in Sr_2RuO_4, Physical Review Letters 83 (16) (1999) 3320–3323. doi:10.1103/PhysRevLett.83.3320.

[4] F. Servant, S. Raymond, B. Fåk, P. Lejay, J. Flouquet, Two-dimensional spin fluctuations in Sr_2RuO_4, Solid State Communications 116 (9) (2000) 489–493. doi:10.1016/S0038-1098(00)00364-1.

[5] B. J. Kim, H. Ohsumi, T. Komesu, S. Sakai, T. Morita, H. Takagi, T. Arima, Phase-Sensitive Observation of a Spin-Orbital Mott State in Sr_2IrO_4, Science 323 (5919) (2009) 1329–1332. doi:10.1126/science.1167106.

[6] M. Braden, O. Friedt, Y. Sidis, P. Bourges, M. Minakata, Y. Maeno, Incommensurate Magnetic Ordering in $Sr_2Ru_{1-x}Ti_xO_4$, Physical Review Letters 88 (19) (2002) 4. doi:10.1103/PhysRevLett.88.197002.

[7] J. E. Ortmann, J. Y. Liu, J. Hu, M. Zhu, J. Peng, M. Matsuda, X. Ke, Z. Q. Mao, Competition between antiferromagnetism and ferromagnetism in Sr_2RuO_4 probed by Mn and Co doping, Scientific Reports 3 (2013) 1–7. doi:10.1038/srep02950.

[8] M. Zhu, K. V. Shanavas, Y. Wang, T. Zou, W. F. Sun, W. Tian, V. O. Garlea, A. Podlesnyak, M. Matsuda, M. B. Stone, D. Keavney, Z. Q. Mao, D. J. Singh, X. Ke, Non-Fermi surface nesting driven commensurate magnetic ordering in Fe-doped Sr_2RuO_4, Physical Review B 95 (5) (2017) 2–7. doi:10.1103/PhysRevB.95.054413.

[9] P. Steffens, O. Friedt, Y. Sidis, P. Link, J. Kulda, K. Schmalzl, S. Nakatsuji, M. Braden, Magnetic excitations in the metallic single-layer ruthenates $Ca_{2-x}Sr_xRuO_4$ studied by inelastic neutron scattering, Physical Review B 83 (5) (2011) 1–12. doi:10.1103/PhysRevB.83.054429.

[10] J. Kwon, B. S. Kim, M. K. Kim, J. Denlinger, A. Bostwick, E. Rotenberg, N. Lee, H. Y. Choi, J. Y. Moon, Y. J. Choi, J. Mun, M. Kim, Y. Yoshida, W. Kyung, C. Kim, Spin-orbit coupling driven orbital-selective doping effect in $Sr_2Ir_{1-x}Ru_xO_4$, Physical Review B 103 (8) (2021) L081104. doi:10.1103/PhysRevB.103.L081104.

[11] J. L. Schmehr, M. Aling, E. Zoghlin, S. D. Wilson, High-pressure laser floating zone furnace, Review of Scientific Instruments 90 (4) (2019) 043906. doi:10.1063/1.5085327.

[12] F. Lichtenberg, A. Catana, J. Mannhart, D. G. Schlom, Sr_2RuO_4 : A metallic substrate for the epitaxial growth of $YBa_2Cu_3O_{7-\delta}$, Applied Physics Letters 60 (9) (1992) 1138–1140. doi:10.1063/1.106432.

[13] J. S. Bobowski, N. Kikugawa, T. Miyoshi, H. Suwa, H.-s. Xu, S. Yonezawa, D. A. Sokolov, A. P. Mackenzie, Y. Maeno, Improved Single-Crystal Growth of Sr_2RuO_4, Condensed Matter 4 (1) (2019) 6. doi:10.3390/condmat4010006.

[14] Z. Q. Mao, Y. Maenoab, H. Fukazawa, Crystal growth of Sr_2RuO_4, Materials Research Bulletin 35 (11) (2000) 1813–1824. doi:10.1016/S0025-5408(00)00378-0.

[15] N. Kikugawa, A. P. Mackenzie, Y. Maeno, Effects of in-plane impurity substitution in Sr_2RuO_4, Journal of the Physical Society of Japan 72 (2) (2003) 237–240. doi:10.1143/JPSJ.72.237.

[16] Q. Zhao, J.-H. Sim, Z. Zhang, H. Su, F. Han, Q. Zhang, B. Tian, Q. Xu, M.-J. Han, C.-G. Duan, J. F. Mitchell, Tetrahedral coordination and low-spin configuration in a 5*d* oxide, Physical Review Materials 3 (6) (2019) 063607. doi:10.1103/PhysRevMaterials.3.063607.

[17] C. Dhital, T. Hogan, W. Zhou, X. Chen, Z. Ren, M. Pokharel, Y. Okada, M. Heine, W. Tian, Z. Yamani, C. Opeil, J. S. Helton, J. W.

Lynn, Z. Wang, V. Madhavan, S. D. Wilson, Carrier localization and electronic phase separation in a doped spin-orbit-driven Mott phase in $Sr_3(Ir_{1-x}Ru_x)_2O_7$, Nature Communications 5 (2014) 1–7. doi:10.1038/ncomms4377.

[18] C. McDaniel, S. Schneider, Phase relations in the Ru-Ir-O_2 system in air, Journal of Research of the National Bureau of Standards 73A (2) (1969) 213. doi:10.6028/jres.073a.019.

[19] A. Kanbayasi, Magnetic properties of $SrRuO_3$ single crystal, Journal of the Physical Society of Japan 41 (6) (1976) 1876–1878. doi:10.1143/JPSJ.41.1876.

[20] A. Biswas, Y. W. Lee, Y. H. Jeong, Electronic and magnetic transitions in perovskite $SrRu_{1-x}Ir_xO_3$ thin films, Journal of Applied Physics 118 (9) (2015) 095303. doi:10.1063/1.4929966.